Passive Low-Energy Nuclear-Recoil Detection with Color Centers

Bernadette K. Cogswell[1,*], Apurva Goel[2,†] and Patrick Huber[1,‡]

[1]*Center for Neutrino Physics, Physics Department, Virginia Tech, Blacksburg, Virginia 24061, USA*

[2]*Department of Physics and Department of Astronomy, University of Washington, Seattle 98105, USA*

Crystal-damage events such as tracks and point defects have been used to record and detect radiation for a long time and recently they have been proposed as a means for dark-matter detection. Color centers can be read out optically and we propose a scheme based on selective plane illumination microscopy for micrometer-scale imaging of large volumes corresponding to kilogram mass detectors. This class of detectors would be passive and would operate at room temperature and we call this the passive low-energy optical color-center nuclear-recoil (PALEOCCENE) detection method. We apply these concepts to the detection of reactor neutrinos using coherent elastic neutrino nucleus scattering (CEνNS). Crystal-damage formation energies are intrinsically on the order of 25 eV, resulting in similarly low nuclear-recoil thresholds. This would enable the observation of reactor-neutrino CEνNS with detectors as small as 10 g. Additionally, a competitive search for spin-dependent dark-matter scattering down to a dark-matter mass of 0.3 GeV could be possible. Passive crystal detectors might also be attractive for nuclear-nonproliferation safeguards if used to monitor reactor power and to put limits on plutonium production. The passive nature and small footprint of the proposed detectors implies that these might fit well within accepted reactor-safeguards operations.

I. INTRODUCTION

The detection of low-energy nuclear-recoil events is one of the frontiers of experimental particle physics. It was studied by Drukier and Stodolsky [1], who were looking for a method to detect coherent elastic neutrino nucleus scattering (CEνNS). This in turn inspired the idea of looking for dark matter by direct detection of nuclear recoils [2]. The present push for nuclear-recoil thresholds of less than 1000 eV is due to our current understanding of dark matter, which has evolved from a classical electroweak-scale weakly interacting massive particle (WIMP) with $m_\chi \sim 100$ GeV to a much broader class of candidates, many with mass 1 GeV or smaller [3]. This, in turn, puts a premium on the smallest possible nuclear-recoil thresholds. At the same time, CEνNS, which was postulated in the 1970s by Freedman [4], has been discovered in 2017 [5] using 50-MeV neutrinos. A pivotal next step is to demonstrate a measurement of CEνNS with reactor neutrinos of around 4 MeV in neutrino energy. On this front, a large number of CEνNS experiments are under way: coherent neutrino nucleus scattering (CONUS) [6], Mitchell Institute neutrino experiment at reactor (MINER)

[7], Nucleus [8], Russian emission detector (RED-100) [9], neutrino elastic scattering observation with NaI[TI] (NEON) [10], Ricochet [11], Taiwan experiment on neutrino (TEXONO) [12] and coherent neutrino-nucleus interaction experiment (CONNIE) [13]. This strong interest in reactor-based CEνNS detection arises from both basic physics [14–18] and potential applications to reactor monitoring for nuclear security [19–21].

The idea of using crystal damage as a detection modality for nuclear recoils has been developed for dark-matter searches [22] and subsequently explored both for damage tracks [23,24] and point defects [25,26]. The results presented here are an adaptation of these prior findings to reactor-neutrino CEνNS and a refinement of some of the prior calculations. Track-based detection faces severe challenges, due to the very low energy of nuclear recoils from reactor neutrinos, and so we focus on point defects, specifically color centers. Color centers have attracted attention in quantum information science [27] and metrology [28] since they can be individually detected by fluorescence spectroscopy. We introduce an optical nondestructive readout scheme based on so-called light-sheet microscopy, also known as selective plane illumination microscopy (SPIM) [29], which is scalable to kilogram quantities of detector material. The resulting detectors are passive room-temperature subkilogram systems with applications to direct dark-matter searches, CEνNS detection

* bkcogswell@vt.edu

† goelapurva1@gmail.com

‡ pahuber@vt.edu

of reactor neutrinos, and reactor monitoring for nuclear-nonproliferation and treaty verification.

In any experiment aiming at low-energy recoil detection, be it for dark-matter searches or reactor CEνNS, it is backgrounds that set the scale for sensitivity and the required effort. Our proposal is no different in this context. We would like to stress that nuclear-recoil backgrounds at nuclear-recoil energies of less than a few hundred electronvolts, the range we are considering here, are essentially a *terra incognita* and the focus of intense experimental efforts. Many experiments do see a sharp increase in their background rate toward this region in energy and this trend seems to apply to many different detector technologies, materials, and shielding configurations [30]. If the cause of this increase is indeed genuine nuclear recoils caused by neutrons, then CEνNS detection at reactors may turn out to be very difficult or even impossible, entirely *independent* of the employed detection technology. We therefore show all our results as a function of the background rate.

In Sec. II, we discuss the formation mechanisms for permanent crystal damage, describe our simulations, and introduce the general features for nuclear-recoil detection. We also present a readout scheme and derive criteria for material selection. In Sec. III, the results for direct dark-matter searches, CEνNS detection at reactors, and reactor monitoring are presented. We conclude with a summary and outlook in Sec. IV. In the Appendix, we provide a detailed calculation of the required parameters.

II. CRYSTAL DAMAGE

A recoiling nucleus will eventually lose all of its kinetic energy to the host crystal lattice via a combination of primarily:

(1) *Phonons*. A collision between the ion and one of the crystal atoms will result in the creation of phonons, which then quickly dissipate. Hence, they are not suitable for the discussion here, except in that any energy deposited in phonons is not available for ionization or lattice defect creation.

(2) *Ionization*. The interaction of the electric field of the moving ion and the electrons in the crystal can displace electrons from their lattice sites, creating a net surplus of positive charge. In an insulator, electrons cannot move to fill in these regions of excess positive charge. The precise mechanism by which ionization creates a permanent track that can, for instance, be made visible by etching is not entirely clear. One possible explanation is that the interaction of these positive charges with themselves and with the rest of the crystal induces mechanical strain. It is thought that it is this strain that weakens chemical bonds [31].

(3) *Lattice-defect creation*. In cases where the energy transfer to a crystal atom exceeds the binding energy in the crystal, the atom can be dislodged from its lattice site and can start to move through the crystal. This can result in a vacancy in the crystal lattice. If sufficient kinetic energy remains in the recoiling atom, it can create a secondary damage cascade, inducing further vacancies.

The use of lattice defects for dark-matter detection has been explored by several authors [25,26]. In addition, the use of ionization tracks has been investigated in a series of papers [23,24]. More recently, ionization track detectors have been proposed to study supernova neutrinos [32] and the time evolution of solar [33] and atmospheric [34] neutrino fluxes. Here, we extend these aforementioned results by performing detailed simulations using the TRIM software package [35] and specifically apply these results toward CEνNS with reactor neutrinos.

Track-based detection has been studied in considerable detail [23,24]; thus, we refer the reader to these references for the underlying formation mechanism. Also, as we discuss in Sec. A, for recoil energies below a few hundreds of electronvolts, track detection hits practical limitations since the resulting tracks are very short (< 5 nm).

Nuclear recoils can lead to the displacement of an atom from its lattice site. This site can remain unoccupied, leading to a vacancy, or it can be filled either by the initial projectile or by some other dislocated atom, in the case of a larger recoil cascade. These are the primary mechanisms for radiation damage from neutron irradiation and, thus, are highly relevant for nuclear engineering. Neutron damage to the reactor vessel is ultimately the limiting factor for the lifetime of a nuclear-fission reactor and for future fusion reactors as well. In our exposition, we follow the review in Ref. [36]. Frenkel defects, where an atom leaves its lattice site and becomes interstitial, occur naturally in crystals at nonzero temperatures. The lifetime of the these defects is short, since lattice strain associated with the existence of the Frenkel defect will lead to spontaneous recombination.

A permanent vacancy forms when the atom is removed far enough from its lattice site so that recombination is no longer possible. This distance is on the order of 1–2 nm. Since the stopping power for most ions is around 20–100 eV/nm, an approximate energy in the range 20–200 eV is required for the creation of a permanent vacancy. This energy is, at best, indirectly related to the binding energy of a given solid or the defect formation energy.

It makes sense to introduce the concept of a threshold damage energy (TDE), with the idea that below the TDE no permanent vacancies are formed. In reality, the situation is more complicated, since the energy required is not isotropic. Also, thermal effects cannot be entirely neglected. Within the simple model of a TDE, denoted as E_d, the number of vacancies n_v formed would be 0 for $T_d < E_d$, 1 for $E_d \leq T_d < 2E_d$, and so forth. Note that T_d is usually called the damage energy, i.e., the kinetic energy remaining in the projectile after all ionization losses have been accounted for. Kinchin and Pease demonstrated in

1955 [37] that this would be too simplistic and that a better approximation is given by $n_v = T_d/(2E_d)$ for $T_d \gg E_d$. This can be intuitively understood by the fact that, for large deposited energies, the crystal melts locally and then recrystallizes. Thus, the final number of surviving defects can be much smaller than the above estimates would indicate. We are interested in very low recoil energies (< 1 keV); thus, this effect can be neglected.

The most accurate calculations are based on molecular-dynamics (MD) simulations and fall outside the scope of our work here. Measurements and molecular-dynamics calculations indicate that the idea of a sharp threshold at which the defect-formation probability discontinuously jumps from 0 to 1 is not accurate. In reality, the defect-creation probability evolves continuously, becoming nonzero well below the TDE and getting close to unity for values of $T_d \sim 2 - 3E_d$. Here, we employ TRIM, a binary collision simulation [35], using full cascades [38]. Note that the following analysis depends quantitatively on these details and the precise number of predicted vacancies as a function of energy. However, the qualitative features of the analysis are quite robust. Relative to earlier work regarding defect formation due to low-energy nuclear recoils [25], we would like to remark that we employ a more detailed calculation based on TRIM of defect formation in relation to recoil energies, generally resulting in higher thresholds than previously found. However, TRIM does not allow us to consider any anisotropy in response, which likely will lead to a moderate increase in the variance of the number of vacancies formed at fixed recoil energy [39].

The TDE has been measured for a number of elements (see, e.g., Ref. [40]) but we are interested in a number of compounds for which no such data can be found. Heuristically, the TDE is found to scale with the melting point of a material [41]. While this scaling is only approximate, it serves as a useful starting point. We find from the information given in Ref. [41] that

$$E_d(T_m) = 0.018 \text{ eV} \left(\frac{T_m}{\text{K}} \right) + 7.2 \text{ eV}, \qquad (1)$$

which is obtained from a fit to 24 data points, and the goodness of fit is 0.23, where T_m is the melting point. This is only a rough approximation and a dedicated measurement and/or computation of this parameter is needed for the specific material in question.

The method of choice to compute the TDE is MD simulations, which also allows the study of the anisotropy of vacancy formation. Crystal damage in CaF_2 has been proposed for neutron dosimetry [42] and, thus, been studied in detail using LAMMPS, a molecular dynamics software program [43]. In Ref. [44], the TDE averaged over all crystal directions is found to be 23 eV, whereas, using the above heuristic, we find the TDE to be 36 eV. This indicates that

our heuristic and the TRIM calculations are, overall, not very far off. Ultimately, the threshold behavior of color-center formation will need to be mapped; for instance, by scattering neutrons of known energy and momentum transfer.

A. General features of crystal defects from CEνNS

In Fig. 1, we show a set of 50 neutron (red) events and 50 reactor CEνNS events (blue) in NaI. The lines are the tracks caused by the primary recoil and the dots are the vacancies created. On average, neutron events are much larger spatially than CEνNS events, since the mean recoil energy is large due to the $1/E$ neutron spectrum, whereas CEνNS events are, on average, only a few nanometers across, since the antineutrino spectrum ends at around 8 MeV. The rate of vacancy formation, n_v, is driven by the TDE, E_d. At large recoil energies, E_r roughly scales as $n_v \propto E_r/2E_d$. Coherent cross sections, either for neutrinos or dark matter, are proportional to the atomic mass squared, A^2, whereas neutron-scattering cross sections are essentially independent of A. For CEνNS, this leads to a preference for materials with a large mass fraction of high-A elements, whereas for dark-matter scattering, obtaining the largest possible recoil energy by minimizing A is useful. Therefore, a combination of detectors, encompassing different materials with differing atomic masses, would allow the neutron and CEνNS signatures to be statistically separated.

In terms of event rates, the sea-level primary neutron rate from cosmic rays is about one order of magnitude larger than the typical CEνNS signal close to a power reactor. The actual background rate depends on the location and details of the shielding configuration. However, the magnitude of the neutron background changes relatively little as a function of the number of vacancies
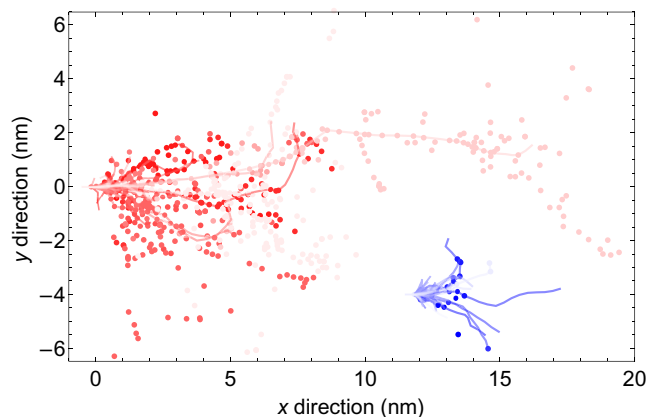

FIG. 1. The overlay of 50 typical cosmic ray neutron (red) and reactor CEνNS events (blue) in NaI. Vacancies are marked by disks and tracks created by the primary recoil are marked by a line.
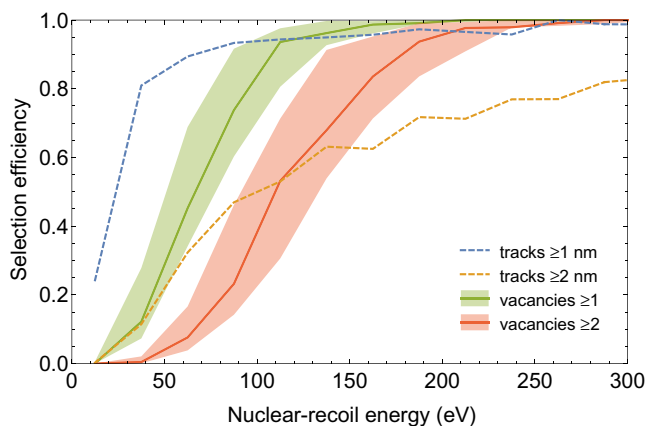
FIG. 2. The nuclear-recoil-energy threshold in NaI for either track-based event selection (dashed lines) or vacancy-based event selection (solid lines). The bands result from a $\pm 20\%$ variation of the threshold damage energy.

created, whereas the magnitude of the CEνNS signal falls steeply with either the number of vacancies or the track length. This indicates that moderate shielding combined with a focus on short tracks and/or few vacancies can help to reduce neutron backgrounds on a statistical basis. To obtain intrinsic rejection of gamma- and beta-radiation backgrounds, we implicitly assume that ionizing radiation does not cause tracks or vacancy formation. Materials have been identified where optically active vacancies result only from nuclear-recoil events [45].

In Fig. 2, we show the resulting nuclear-recoil threshold behavior for track-based (dashed) event selection and vacancy-based (solid) event selection. In all cases, the nuclear-recoil threshold, corresponding to 0.5 efficiency, is less than 100 eV, which is the primary reason why vacancy formation has been considered for dark-matter detection [25]. The difference between this analysis and that in Ref. [25] is that our vacancy threshold function is based on a full TRIM calculation and we find generally higher values (approximately $2E_d$). Also, it becomes apparent that track-based event selection requires the ability to measure approximately 1-nm-long tracks. The methods for track readout discussed in Refs. [23,24] are in principle sensitive to short tracks. However, the rate at which they can scan a volume decreases rapidly for shorter tracks. Moreover, they likely would be destroying the crystal. Therefore, overall, they are not a good fit to the applications proposed here. Also, indirect track detection, via strain-induced frequency shifts in preexisting color centers [26], only applies to tracks longer than a few tens of nanometers. Therefore, for our purposes, we do not consider the track readout option further.

B. Readout schemes

Color centers have been proposed as a useful detection mechanism in the context of direct dark-matter searches

[25]. In particular, so-called F centers are attractive for this application. An F center is a vacancy of the anion in an ionic crystal that traps an electron. The resulting energy levels of this electron-vacancy bound state are amenable to fluorescence, i.e., they can be excited by visible light of a suitable wavelength and the subsequent deexcitation results in the emission of photons. Individual color centers can be detected using confocal microscopy, whereby the excitation and fluorescence light share the same light path; the spatial resolution is approximately 1/2 of the wavelength [46]. The limitation of this method is that when scanning a three-dimensional volume, only one voxel can be acquired at a given time; hence the total volume throughput is low. In Ref. [25], the use of an optical fiber is proposed, which effectively samples the whole volume of the fiber simultaneously, but without any ability to determine the axial position of a defect. Therefore, any preexisting defects that are unavoidable become a background, which has to be subtracted statistically. In a dark-matter context, very small (gram-scale) samples that are exposed over hundreds of millions of years may still yield acceptable sensitivity. However, for applications to reactors, only exposure times of a few years or less are possible and hence large samples (approximately 10–1000 g) are required. This is where the optical nondestructive technique that we propose may become especially useful.

The work in Ref. [25] has led directly to an experimental follow-up study [45]: the authors measured the bulk fluorescence of a number of materials as a function of both the excitation wavelength (250–800 nm) and fluorescence wavelength (300–1200 nm). They compared unirradiated samples, samples that were irradiated with gamma photons from a ^{60}Co source with a dose of up 1.6 Gy and samples that were exposed to neutrons from a ^{252}Cf source with a fluence of roughly 10^{10} cm^{-2}, corresponding to a kerma of about 0.1 Gy. For some materials, it can be shown that color centers are selectively formed only by neutron irradiation and not by gamma irradiation. These materials and their excitation (fluorescence) wavelengths are as follows: Al$_2$O$_3$, 250 (400) nm; SiO$_4$, 250 (346) nm; LiF, 260 (331) nm; BaF$_2$, 250 (270) nm. Note that both LiF and BaF$_2$ are candidate materials for the technique discussed here, as explained in detail in Sec. C. Moreover, these data allow us to put an upper limit on the intrinsic preexisting color-center density in those materials at the $10^{-12} - 10^{-10}$ level (see the Appendix). No other optical backgrounds are apparent from these data. We also learn from these data that color centers with different excitation and/or fluorescence wavelengths combinations exist within the same material and that some do respond to gamma radiation while others do not.

We propose the use of light-sheet microscopy, also known as SPIM [47], which is an evolution of confocal microscopy wherein the excitation light and fluorescence light paths are orthogonal to each other. A sheet of light
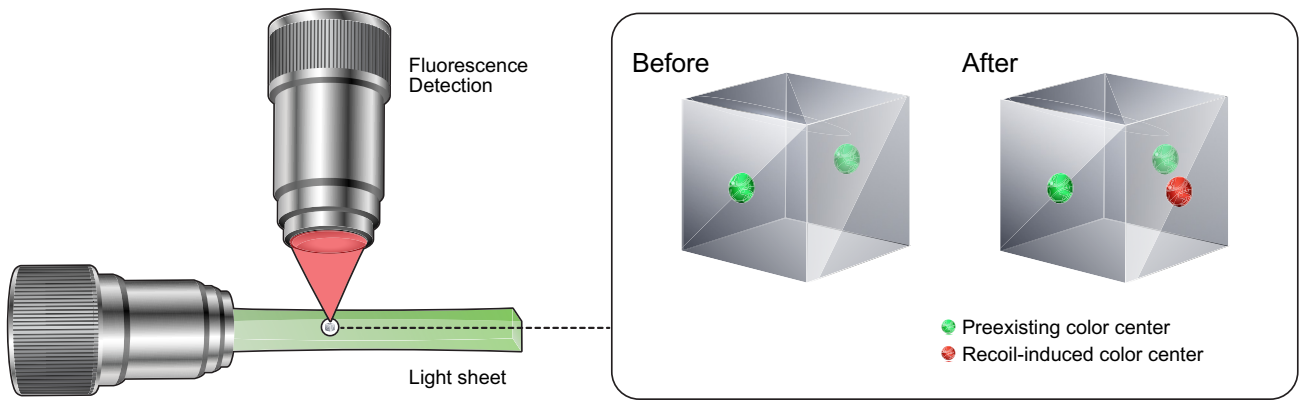
FIG. 3. A schematic layout of the light-sheet microscopy used for imaging single color centers prior to and post exposure.

illuminates the entire field of view of the fluorescence light path and, thus, as many voxels as there are pixels in the camera along the fluorescence light arm can be imaged simultaneously (see Fig. 3). For a review of this technique, see, e.g., Ref. [29]. For biological systems, there is an interest in observing dynamic processes in whole organisms; hence repeated fast sampling of a relevant volume is desired. One potential technology for this purpose is spherical-aberration-assisted extended depth-of-field (SPED) light-sheet microscopy [48]. The point spread function of the fluorescence light path is extended so that a large volume can be imaged. With SPED, imaging of 12 volumes of $0.9 \times 0.4 \times 0.2$ mm^3 per second has been demonstrated, which translates to 75 cm^3 per day. This volume is scanned in 40 steps in the z direction, making each z slice 5 μm thick, and the time per slice is $1/(40 \times 12) \simeq 2$ ms. Hence, this technique allows volume sampling in the range of $50 - 100$ cm^3 per day.

If we assume $\mathcal{O}(1)$ preexisting defects per voxel (corresponding to a defect density of 10^{-10} defects per atom, which is the upper limit derived from the data in Ref. [45]), only a relatively small number of fluorescence photons need to be acquired to obtain positive detection of a new defect. To achieve a false positive defect detection rate of 10^{-12}—that is, roughly only one false positive for the entire detector—and assuming one preexisting color center per voxel, about 100 photons are required to conclusively detect the presence of one additional defect. If we suppose an oscillator strength of order 1 for the color center, we end up with an absorption cross section of approximately 10^{-17} cm^2 [25]. Accounting for the quantum efficiency of the camera and the light-collection efficiency of the objective, we find the following parameters for scanning 100 g of BaF$_2$: a laser power of 12 W, a temperature rise in the 1-mm-thick sample of 3.4 K, and a data volume of 41 TByte; for details, see the Appendix, where we also give the appropriate scaling laws. From this discussion, it follows that the number of preexisting color centers of the type induced by nuclear recoil is a key figure of

merit for any material and will need to be experimentally determined.

Moreover, the crystal could be imaged prior to deployment and, thus, a voxel-by-voxel subtraction of background is feasible, as shown in Fig. 3 At the same time, the comparison of pre- and postdeployment images serves to verify the identity of the crystal and that it has not been tampered with—by, for instance, heating it to anneal defects. These features, in combination, allow for single-event detection.

C. Materials selection

Existing studies and physics considerations help identify six material candidates. In terms of material properties, we propose that acceptable candidates meet the following criteria:

    (a) Have a melting point well above room temperature

    (b) Be an electrical insulator

    (c) Permit optically active defects (color centers)

    (d) Have color centers that are selectively formed by nuclear recoils, only

    (e) Be able to produce optical quality crystals

    (f) Contain high-mass (for CEνNS) or low-mass (for dark matter and neutrons) elements

    (g) Have a low TDE

Color centers, i.e., crystal defects that are optically active, are common and were discovered in rock salt (NaCl). They are known to exist in all chemical group I–VIII compounds. Color centers are not confined to this group of compounds, however, and are found in many materials, including glasses. For LiF and BaF$_2$, color centers have been confirmed to be selectively created only by neutron and not gamma irradiation [45]. That is, LiF and BaF$_2$ detectors will be immune to ionizing radiation. The cited study of these two materials has been specifically performed with the goal of dark-matter detection. Also, color centers in NaI [49], CsI [50], CaWO$_4$ [51], and Bi$_{12}$GeO$_{20}$

TABLE I. The materials considered in this study. A is the atomic mass of the heaviest element and m_A the corresponding mass fraction. TDE is the threshold damage energy, $E_{1/2}$ is the nuclear-recoil energy at which half of the asymptotic efficiency is reached. CEνNS event numbers are computed for 100 g of target and 1-year exposure at 10 m from a 3-GW$_{th}$ reactor. The same number for inverse beta decay on CH_2 is 1250. The selection efficiency is the fraction of reactor CEνNS events that have one or more vacancies created. The usable events are the number of events where one or more vacancies are created.

Material	A (u)	m_A (%)	Density (g cm^{-3})	Melting point (K)	TDE (eV)	$E_{1/2}$ (eV)	CEνNS events	Selection efficiency (%)	Usable events
LiF	19.0	73.2	2.64	1 120	27	80	5 600	75	4 200
BaF$_2$	137.3	78.3	4.88	1 625	35	105	48 800	20	9 600
NaI	126.9	85.0	3.67	935	24	65	46 900	32	15 100
CsI	132.9	~ 100	4.51	900	23	55	55 700	37	20 600
CaWO$_4$	183.8	63.9	6.06	1 895	41	110	55 400	8	4 600
Bi$_{12}$GeO$_{20}$	209.0	86.4	9.22	1 175	28	85	83 500	17	14 000

(BGO) [52] have also been observed in response to x-ray and electron irradiation. However, specific studies to determine if a neutron-gamma separation, as in LiF, is possible are required for these other four proposed materials.

The neutron cross section is more or less independent of the atomic mass, A, whereas the CEνNS cross section scales with A^2. Therefore, heavy elements are preferred. Within the group I–VIII compounds, this makes NaI and CsI prime candidates. Therefore, in terms of finding an ideal material, we look for the heaviest possible elements and materials with the largest possible concentration of those heavy elements. Two candidates that fit this description are CaWO$_4$ and BGO. Both materials appear in nuclear- and particle-physics applications as scintillators and/or low-temperature bolometers. This implies their ready availability (and relative affordability) as large (hundreds of grams) crystals with good optical qualities and a low radioactive impurity content. With bismuth and tungsten being at the upper range of atomic masses for stable elements, and given the large weight fraction of these in the above compounds, it at first appears, theoretically, that these two materials would be the most attractive target materials.

The results from the TRIM simulation, for the six materials identified, are shown in Table I. While the simple argument given above bears out for the actual number of CEνNS events, looking at the fraction of reactor CEνNS events that produce one or more vacancies, we can see that the number of actual usable events does not follow this simple trend. LiF does remarkably well in this metric compared to CaWO$_4$. LiF has a fairly high value of $E_{1/2}$ but also the mean recoil energy from reactor CEνNS events is large, so that the selection efficiency is 75%. For CaWO$_4$, on the other hand, the mean recoil energy from reactor CEνNS events is small and, hence, the selection efficiency is only 8%. The selection efficiency for one or more vacancies created is well below unity, which would be much less of a problem in a track-based analysis, i.e., many more events leave tracks of 1 nm or longer. However,

the neutron background rises very steeply at the lowest energies and, thus, these very low-energy events are not very useful. We confirm this by computing the same results as shown in Figs. 5 and 6 with a track-based selection for events (with tracks of 1 nm or longer) and obtain virtually identical results. Given our inability to find a convincing readout scheme for tracks that are short, we do not include these results here. Note also that high-mass materials offer a better distinction of their CEνNS events from neutrons, since their signal peaks at low energies—that is, few events will create multiple vacancies—whereas the neutron-vacancy distribution is nearly independent of the atomic mass. For the same reason, LiF, despite its usable-event number being comparable to that for CaWO$_4$, does quite poorly as a reactor CEνNS detector; the shapes of the signal and background distributions are too similar.

We would also like to remark that the results of Ref. [21] are confirmed in our analysis: thresholds of a few hundred electronvolts or less are needed to gain any advantage relative to inverse beta decay in the event rate per unit mass. For the six materials in Table I, we find a mass advantage on usable events of 3.3–16. Mass advantage is defined as the ratio of the mass of an inverse-beta-decay- (IBD) based detector to the mass of a CEνNS-based detector, at the same performance [21].

For dark-matter detection, the considerations are somewhat different. Dark-matter detectors are located deep underground. Consequently, neutron backgrounds are of less concern. Neutron-background-free measurements up to an exposure of tens of kilogram years have been reported (see e.g., Ref. [53]). As we discuss in detail later, LiF is an ideal material because of its very low atomic mass and because both Li and F have a net nuclear spin.

III. RESULTS

A. Dark-matter detection

There is ample evidence for dark matter based on the dynamics of galaxies and galaxy clusters as well as

from precision cosmology [3]. Assuming that some new species of particles is responsible for these results, a picture emerges where the Milky Way, like all other galaxies, is embedded in a dark-matter halo and the Sun's orbit around the center of the Milky Way leads to an effective dark-matter wind. Dark matter being dark, i.e., electrically neutral, the most plausible detection mechanism is the creation of nuclear recoils via some new interaction [2]. We broadly follow the description in Refs. [54,55] in order to compute the expected event rate for dark-matter scattering in our detectors as well as the recoil-energy spectrum. The detection mode discussed here is relevant for spin-dependent interactions and given as [55]

$$\frac{d\sigma_\chi}{dq^2} = \frac{F^2(q)}{4\mu_A^2 v^2} \frac{32 G_F^2 \mu_A^2}{\pi} \frac{J+1}{J} \left(a_p \langle S_p \rangle + a_n \langle S_n \rangle \right)^2, \quad (2)$$

where μ_A is the reduced mass of the colliding system, $a_{p/n}$ are the spin-dependent coupling to the proton and neutron, respectively, J is the total nuclear spin, and $\langle S_{p/n} \rangle$ are the average proton and neutron spins in the nucleus. $F^2(q)$ is the nuclear form factor, which we set to 1 since we are interested in sub-kiloelectronvolt recoils only. To evaluate the spin-dependent cross section, we use for ^{19}F the proton-coupling $\langle S_p \rangle = 0.477$ [55]; for ^{7}Li, we use $\langle S_p \rangle = 0.497$ [56] and we set $\langle S_n \rangle \simeq 0$ for both isotopes. Here, v is the velocity of the dark-matter particle in the laboratory frame. Therefore, this cross section needs to be integrated with respect to the dark-matter velocity distribution, which is assumed to follow a truncated Maxwell distribution with $v_0 = 230$ km s^{-1} and a cut-off of $v_{esc} = 600$ km s^{-1}. Also, we use $\rho_0 = 0.4$ GeV cm^{-3}. The maximum nuclear-recoil energy is given by

$$E_{max} = \frac{4 M_\chi M_A}{(M_\chi + M_A)^2} \frac{1}{2} M_\chi v_{esc}^2, \quad (3)$$

which yields $E_{max} \simeq 40$ eV for $A = 7$ and $M_\chi = 0.25$ GeV. For spin-independent dark-matter couplings, our detection scheme is unlikely to provide a relevant advantage, since very low-threshold silicon [dark matter in CCDs (DAMIC), sub-electron noise skipper CCD experimental instrument (SENSEI)] and germanium [super cryogenic dark matter search (SuperCDMS)] detectors are already available [13,57,58].

To optimize the sensitivity to spin-dependent dark-matter couplings, nuclei with a net total nuclear spin are required. To optimize the sensitivity to small dark-matter masses, light nuclei are preferred. This makes LiF a good candidate material [45]. Both ^{7}Li and ^{19}F have a net nuclear spin of 1/2 and sizable average proton spins. They are also both rather light. ^{19}F is the single stable isotope of fluorine and ^{7}Li has an isotopic abundance of 92.4%. Consequently, both elements have been used to set limits on spin-dependent dark-matter couplings [56,65]. In Fig. 4,
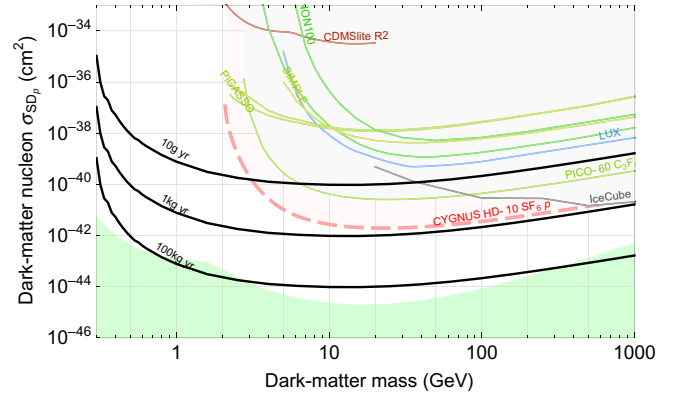

FIG. 4. The 95% confidence-limit (CL) sensitivity with LiF for spin-dependent dark-matter scattering (black lines) for different exposures, assuming a background-free experiment. The green shaded region is the neutrino floor for LiF. All other experiments and exclusion limits have been plotted using Ref. [59], specifically SIMPLE II [60], PICO-60 [53], LUX [61], Panda-X II [62], XENON-100 [63], and CDMSlite [64].

we show the results for various exposures of LiF, where our exclusion limit is defined by requiring 2.3 events. We assume that the experiment is otherwise background free. Given the experience of the PICASSO and COUPP collaboration experiment (PICO-60) [53,56] and extrapolation to the PICO-500 [66], our assumption seems plausible for target masses up to 10 kg even in the absence of a muon veto.

In producing these limits, we compute the recoil spectrum for a given dark-matter mass for both Li and F and use TRIM to compute the resulting number of vacancies. Hence, we can select all events that have one or more vacancies. The neutrino floor is computed using neutrino fluxes for solar and atmospheric neutrinos [67] as described in Ref. [68]. This neutrino floor would be reached for exposures of around 100 kg yr. Given an estimated readout rate of 100–200 g per day, exposures above approximately 10 kg yr will require moderate scaling of the readout rate, which is probably best accomplished by using several microscopes in parallel. Note that the readout for the dark-matter detection has to happen underground, because neutron backgrounds at the surface would overwhelm any signal in this case. The resulting exclusion limits that we find in our analysis are unmatched for dark-matter masses below 3 GeV and extend down to 0.3 GeV, representing a one-order-of-magnitude improvement in mass reach.

B. Reactor CEνNS

CEνNS occurs when a neutrino interacts coherently with the total weak nuclear charge (necessarily at low momentum transfer), leaving the ground-state nucleus to recoil elastically [4]. It was observed in 2017 with 50 MeV

neutrinos from the Spallation Neutron Source (SNS) at Oak Ridge [5].

The CEνNS cross section is enhanced by N^2, where N is the neutron number and can thus exceed IBD cross sections by more than 2 orders of magnitude per unit detector mass. However, this advantage can only be realized for very small recoil-energy detection thresholds [21]. The standard model cross section for coherent elastic neutrino scattering is given by [4]

$$\frac{d\sigma}{dT}(E_\nu, T) = \frac{G_F^2}{4\pi} N^2 M \left(1 - \frac{MT}{2E_\nu^2}\right), \qquad (4)$$

where G_F is the Fermi constant, M is the total mass of the nucleus, T is the nuclear-recoil energy, and E_ν is the neutrino energy. Due to the low energy of reactor neutrinos, we can safely set the nuclear form factor to 1. For a given neutrino energy, kinematics limits the recoil energy to be less than

$$T_{\max} = \frac{E_\nu}{1 + \frac{M}{2E_\nu}}, \qquad (5)$$

which for a target mass $A = 100$ and $E_\nu = 8$ MeV equates to about 1200 eV and for $E_\nu = 1$ MeV to about 20 eV, which are typical energy endpoints for reactor-neutrino fluxes. These very small nuclear-recoil energies are the reason that CEνNS has not yet been observed at reactors. The number of interactions is given by

$$n = \frac{G_F^2}{4\pi} M \int_T^{T\max} \int_0^\infty dE_\nu \times \phi(E_\nu) N^2 \left(1 - \frac{MT}{2E_\nu^2}\right), \quad (6)$$

where $\phi(E_\nu)$ is the reactor-neutrino flux, which we obtain from a summation calculation performed following the formalism outlined in Ref. [69] down to a neutrino energy of 250 keV. For simplicity, we assume a reactor running on pure ^{235}U. More realistic fission fractions would change the event numbers by less than 20%. Neutrinos from neutron capture reactions on ^{238}U [19] cause recoils that are below the energy threshold considered here and can be safely neglected.

There are a large number of experiments under way aiming to be the first to detect CEνNS at a reactor using more complex and higher-maintenance methods than the one proposed here: CONUS, using cryogenic (70-K) germanium detectors [6], MINER, using cryogenic (15-mK) germanium detectors [7], NUCLEUS, based on cryogenic (15-mK) CaWO$_4$ bolometers [8], RED-100, a dual-phase liquid-xenon (170-K) detector [9], NEON NaI scintillator detectors [10], RICOCHET low-temperature bolometers (15-mK) [11], TEXONO cryogenic germanium (70-K) detectors [12], and CONNIE, using silicon CCDs at 100 K [13]. Notably, only NEON operates at room temperature.

However, the only experiments to demonstrate nuclear-recoil thresholds below 100 eV are bolometers operating at millikelvin temperatures.

In light of the current lack of understanding of recoil background at the low energies relevant here, we would like to emphasize that the detection method we propose is in general not more or less affected by genuine neutron backgrounds than existing technologies. The one exception is muon-induced events, which in principle can be reduced using an active muon veto. Since this requires event timing information, which our technology cannot provide, this option is not available. On the other hand, should the observed low-energy excess [30] be due to yet-to-be-understood energy depositions in the detector not related to nuclear recoil, the technology we propose here could help to disentangle these unknown contributions. Existing detector technologies ultimately measure an energy deposition, which in principle can have many sources: in our proposal, we measure the creation of very specific crystal defects in the form of color centers at a microscopic level.

Cosmic ray neutron backgrounds cannot be avoided for a close-to-surface deployment. Neutron recoils produce exactly the same type of recoil as the CEνNS reaction and, thus, are the leading source of background. For our purposes, recoils with energies in the 100–1000 eV range are most relevant. Hence, neutrons in the 100–10 000 eV range cause the relevant background events. Neutrons at the surface of the Earth are predominantly produced by cosmic ray interactions within the atmosphere. Cosmic ray muons interacting in materials close to the detector can also produce neutrons. In practice, a fine balance between these two background sources will need to be achieved. For shielding thicker than a few meters water equivalent muon interactions inside the shielding itself become the dominant source of neutrons. A detailed understanding of neutron backgrounds and the effectiveness of shielding will require a careful simulation of the specific setup and materials. Ultimately, only an actual measurement can settle the issue.

Neutrons in the energy range of concern, 100–10 000 eV, can be effectively shielded in surface environments. Shielding factors of up to 100 have been demonstrated with shields of an areal density less than 100 g cm^{-2} [70]. A similar result is found in the context of upcoming and ongoing CEνNS experiments at reactors [6,71–75]: typical background rates at the surface of around 10 000 events per day and per kilogram of detector in the energy range from 20 to 10 000 eV are stipulated. This agrees well with our simplified model. Therefore, it appears at least possible that passive shielding could yield a suppression factor of 100. Note that active shielding would require the detector to be read out in real time and thus is not considered here. On the other hand, should the low-energy event excesses reported by a number of experiments indeed be due to genuine recoil events, it would be
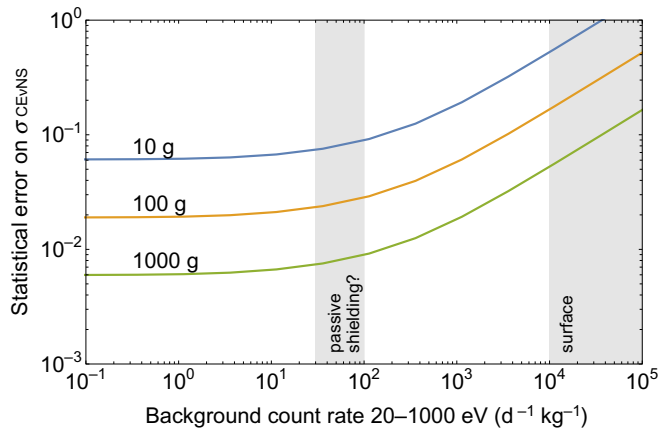
FIG. 5. The 1σ error on the CEνNS cross section obtainable at a nuclear reactor for a variety of detector masses in a vacancy-based counting analysis, as a function of the neutron background rate. The exposure is 1 year at 20 m from a 3-GW$_{th}$ reactor.
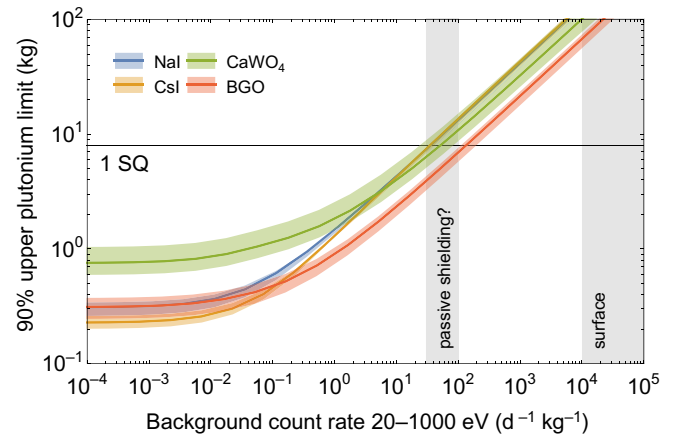

FIG. 6. The 90% CL limit upper bound on the amount of produced plutonium for a reactor that is shut down as a function of the neutron background rate. The detector size is 100 g, the distance is 20 m, and the data-taking period is 90 days. The different curves are for different materials, as specified in the legend, and the width of the band is due to a $\pm 20\%$ variation of threshold damage energy. The black horizontal line indicates 8 kg of plutonium, the so-called significant quantity (SQ).

unclear if backgrounds can be overcome by this, or any other, technique.

In Fig. 5, we show the 1σ error on a measurement of the CEνNS rate at 20 m from a 3-GW$_{th}$ reactor for a 1-year deployment as a function of the neutron background rate. The assumption is made that no reactor-related background from fast neutrons is present. The data and the background recoil rate and spectra are computed as described above and the ensuing recoil spectra are put into TRIM, which then outputs the distribution of produced color centers. The resulting signal and background histograms are used to compute the 1σ error using a maximum-likelihood method. The bin with zero color centers formed is excluded in the analysis, resulting in an overall 32% efficiency (see Table I). In evaluating the likelihood, the normalization of the background is treated as an unconstrained nuisance parameter and profiled over. The result is statistical only; that is, no analysis on reactor-flux systematics or signal normalization is included.

Even a 10-g crystal with moderate shielding could easily achieve a 5-σ detection and 100–1000-g detectors can probe the physics associated with CEνNS well into the regime where reactor-flux systematics will become the limiting factor. NaI is used as an example but many other materials would lead to comparable results (see also Fig. 6). To distinguish the CEνNS signal from backgrounds, three handles are available: the vacancy-number distribution, with neutrons producing a higher mean number of vacancies; the reactor on-off comparison; and codeployment of a high-atomic-mass crystal such as BGO with a low-atomic-mass crystal such as LiF would exploit the different scaling with the atomic mass of the signal and background to uniquely establish the signal as stemming from CEνNS. The materials considered in our study span

the atomic mass range $A = 7$–209, which is also invaluable for testing and discriminating various new physics models.

Neutrino applications to reactor monitoring and nuclear security have been suggested by Borovoi and Mikaelyan [76] around the same time that CEνNS was proposed. Since then, there have been many studies conducted and detectors built with the goal of real-world implementation [20]. However, roadblocks arise from the complexity of neutrino detectors, which are still more like a science experiment than a field-deployable robust device, and the need to deal with cosmic ray backgrounds by going underground. Major excavation is generally considered impossible close to a reactor and only a few reactor sites have an existing suitable underground site. In 2018, the problem of underground neutrino detector deployment was solved by the early demonstrations of surface reactor-neutrino detection [77,78].

The Treaty on the Non-Proliferation of Nuclear Weapons (NPT) is the backbone of efforts in nuclear security and nonproliferation. It includes an extensive verification regime, which is implemented by the International Atomic Energy Agency (IAEA). The IAEA is faced with the task of inspecting more than 400 commercial reactors, and around double that number of research reactors, on a limited and relatively fixed budget. Therefore, a typical neutrino detector, with its cost, ton scale, and several square meters of footprint, floor loading, maintenance requirements, etc., is not a particularly good fit for the IAEA [79].

The detector type that we propose here can, in principle, overcome many of these IAEA implementation

constraints. It is small (subkilogram), cheap, robust, passive, operates at room temperature, is maintenance free, and does not present a fire hazard. Overall, the concept of operations is very similar to tags and seals, which the IAEA already uses, wherein an IAEA inspector would emplace the detector and use a seal to ensure that it stays secure. After a period of time, the inspectors would return, retrieve the detector and ship it to a central laboratory for analysis [80]. A scan of preexisting defects, prior to deployment, would allow for unique identification of the detector crystal when it returns for analysis after a deployment cycle.

This pre- and postimaging analysis can also verify that the detector has not been tampered with. For instance, heating it in an attempt to anneal crystal defects would also reduce the number of preexisting defects and thus be detectable. One scanning station could be used for a large number of detectors. Also, being entirely passive, these detectors are immune from cyber threats. In the case of a cyber attack on conventional systems, they could provide continuity of knowledge or a redundant backup in case of a power outage induced by malicious or climate-change-based catastrophic events. Seals and other passive techniques currently used by the IAEA share this trait but passive CEνNS detectors can additionally provide direct information on reactor operations. Each detector would essentially be only as costly as its materials. Since the materials discussed here are all commercially available, this cost would be relatively low.

In Fig. 6, we show the limit on plutonium production in a reactor that can be obtained with 100 g of various detector materials as a function of the neutron background rate, at a distance of 20 m from reactor output, and within a data collection time of 90 days. The detection goal of the IAEA for plutonium is one significant quantity (1 SQ), defined as 8 kg, within 90 days at 90% probability [81]. The horizontal line labeled "1 SQ" indicates this limit. The width of the bands arises from a ±20% variation of TDE as given in Table I. There is a range of materials which, with moderate shielding, can meet this criterion. Since the detector itself is small, an appropriate shield of about 0.5–1 m thickness still yields a compact device. Also, the passive shield does not need to be moved when the detector is retrieved; it only needs to be put permanently in place once.

Outside of the reactor building (to which a 20-m distance roughly corresponds), a small-diameter, approximately 10-cm, shallow borehole of 1–2 m depth can easily provide the requisite shielding for this passive CEνNS detection method; as could a simple barrel full of water. Codeployment of a low-atomic-mass detection medium such as LiF can serve as an independent background assay. Compared to neutrino detectors based on inverse beta decay, the only ones demonstrated to date, the information content of the signal of the detector proposed here is a rate-only measurement with no time information. That is,

our detectors provide measurements of the total neutrino fluence over the deployment period, with no information on the neutrino energy spectrum. Thus, use cases related to determining the fission fractions in a reactor (see, e.g., Ref. [82]) are not covered.

On the other hand, use cases that only need a total rate measurement can be effectively addressed with the proposed passive CEνNS method; in particular, since the event rate per unit mass is favorable for CEνNS given the very low recoil threshold that we can achieve [21]. One potential use case would be the verification of reactor shutdown and, hence, the absence of plutonium production during a given period. Another use case could be the monitoring of larger research reactors to ensure that the product of reactor power and operation time stays below a certain bound, to exclude their use for plutonium production. For this application, the IAEA is currently using the so-called thermohydraulic power monitor [83], which is used to measure the flow rate of coolant and temperature rise across the reactor. In comparison, the detectors proposed here would be cheaper, easier to install, and would require less maintenance.

IV. SUMMARY AND OUTLOOK

In this paper, we propose using crystal damage caused by nuclear recoils for dark-matter detection and CEνNS detection with reactor neutrinos. We call this technique PALEOCCENE. We perform a detailed simulation of track formation and vacancy creation, using the TRIM software, and present results for six promising candidate materials. In the selected materials, vacancy creation eventually results in the formation of color centers. We propose a readout scheme using selective plane illumination microscopy, which exploits the fluorescence of these color centers. This specific type of microscopy can image 50–100 cm^3 per day at submicron resolution with single color-center sensitivity and has been developed for applications in biology. This also enables imaging of preexisting (unavoidable) color centers. These data can then be used for event-by-event discrimination from color centers created during detector deployment.

This is a major improvement relative to the color-center-based dark-matter and solar-neutrino detection scheme put forward previously in Ref. [25]. In a nuclear-security application, the pattern of preexisting color centers also serves as a unique identification of the specific detector deployed [84] and as a means to identify detector tampering. We also discuss the cosmic ray neutron background for reactor measurements. Neutron backgrounds can be determined *in situ* by either exploiting color-center multiplicity or by codeployment of a low-atomic-mass detector and leveraging the A^2 dependence of CEνNS. We use this analysis framework to study three specific applications:

(1) Direct dark-matter detection with spin-dependent forces in LiF: a 10-g yr exposure would set the world's best limit for dark-matter masses between 0.3 and 3 GeV. Scaled to a 1-kg yr exposure, this detector would set the best limit up to masses of 1000 GeV.

(2) Reactor-neutrino CEνNS discovery in NaI: A 10-g yr exposure at 20 m from a 3-GW$_{th}$ reactor would allow for a more than 5-σ detection of the CEνNS signal. Scaling the exposure to 100–1000 g yr would yield a flux-systematics-limited measurement at the percent level.

(3) Reactor monitoring for nuclear security and treaty verification in NaI, CsI, BaF$_2$, BGO, and CaWO$_4$: We find that the sensitivity to plutonium production conforms to the IAEA detection goals [81], both in terms of timeliness and plutonium quantity, for detector masses as small as 100 g. Given that our system is passive and small, its concept of operation likely fits well within established IAEA workflows and could be an attractive replacement for the thermohydraulic power monitor used at some research reactors. Immunity from cyber threats, combined with a generally unspoofable signal, is another attractive feature for these applications.

For all three examples studied, the detectors would be small (10–1000 g), passive, robust, cheap, and maintenance free. They would operate unsupervised at room temperature with no electronics. Potentially only modest passive shielding might be required.

Furthermore, we note that subgram detectors would make excellent high-sensitivity passive neutron detectors for a wide range of neutron energies. These could be especially well suited for zero-knowledge proof protocols for disarmament verification of nuclear warheads [85,86]. The idea is that a neutron beam interrogates the warhead, but a preloaded neutron image, only known to the owner of the warhead, is superimposed inside the detector. This allows one to verify that several objects are the same without revealing any details about their construction. This approach relies on passive neutron detectors that can be reliably preloaded by the host, can store the neutron information for a long time, and can be read out repeatedly. It appears likely that the detectors proposed here have the requisite combination of properties.

The quality of the simulation performed here and the uncertainty on inputs such as the threshold damage energy, indicate that a follow-up with experimental studies is needed. We consider this as the best way forward. For a proof of concept, next steps would include investigating to what extent color-center formation is selective against gamma rays, which, out of the materials studied here, has been demonstrated only for LiF and BaF$_2$ [45]. An at-scale demonstration of single-color-center imaging, with the requisite resolution and speed, would also be an important next step. Following on would be detailed studies of neutron recoils and the relationship between neutron energy and color-center formation rate, essentially mapping the threshold function. These data could also be used to create validated simulation tools. In combination, these steps would likely allow for an attempt to deploy a detector at a reactor and obtain a first observation of reactor CEνNS in the near future. Since the proposed detector materials and readout systems are commercially available, the necessary R&D program could be relatively fast and cheap to put together.

APPENDIX: PHOTON ECONOMICS, HEATING, AND DATA RATES

To scan a given volume per day, V, several factors need to be considered:

1. Can a microscope system cope with the mechanical needs to scan the volume V at the required rate by repositioning the sample at the requisite precision and focus quickly enough?

2. What is the density of preexisting color centers?

3. What laser power is need to achieve clear detection of color centers in the volume V?

4. Is the resulting heat input into the sample manageable?

5. Is the resulting data rate manageable?

1. Mechanics

To give a specific example, consider spherical-aberration-assisted extended depth-of-field (SPED) light-sheet microscopy as an example [48]. We find that imaging of 12 volumes of $0.9 \times 0.4 \times 0.2$ mm^3 per second has been demonstrated, which translates to 75 cm^3 per day. This demonstrates that the mechanics of scanning a large volume is a solved problem.

2. Preexisting color centers

The results of Ref. [45] allow us to put an upper bound on the intrinsic color-center density in the materials of interest by estimating the number of radiation-induced color centers. Given the neutron flux of $(3.8 - 8) \times 10^4$ cm^{-2} s^{-1}, a neutron scattering cross section between 2 and 4 barns, and an irradiation time of 64.3 h, we obtain $10^8 - 10^9$ neutron interactions per cm^3. Based on a TRIM calculation, this results in about 200–500 vacancies per neutron event with a neutron energy spectrum corresponding to ^{252}Cf, or about $10^{10} - 10^{12}$ color centers per cm^3. Given target-atom densities of few times 10^{22} cm^{-3}, this corresponds to relative radiation-induced color-center abundances of $f_d < 10^{-12} - 10^{-10}$. This number presents a conservative upper bound on the intrinsic color-center abundance.

3. Power

For a material of given molecular weight M and density ρ, there are

$$N = \rho/M N_A \qquad \text{(A1)}$$

target sites per cm^3, where N_A is Avogadro's constant. Assuming a preexisting defect fraction f_d, the density N_p of preexisting defects is $N_P = f_d N$. Defining the volume of a voxel V_{vox} as

$$V_{\text{vox}} = v_x v_y v_z, \qquad \text{(A2)}$$

where v_x, v_y, and v_z are the corresponding voxel dimensions in the x, y, and z directions, the number of defects per voxel D is given by $D = N_d V_{\text{vox}}$.

The number of photons, p emitted by a single color center per unit time is

$$p = \phi \sigma_0 \xi, \qquad \text{(A3)}$$

where ϕ is the photon fluence into the sample, $\sigma_0 = 10^{-17}$ cm^2, and ξ is the oscillator strength. The number of detected photons per unit time p_d is given as $p_d = p \, \text{NA}^2/4 \, \epsilon$, where NA is the numerical aperture of the collection microscope objective and ϵ is the quantum efficiency of the camera.

Next, we need to determine how many photons we need to detect, p_n, to be certain that there is one additional color center in a voxel relative to the number of preexisting color centers D in that voxel. Assuming that the number of photons γ is reasonably large—say, bigger than ten—the Poissonian count-rate statistics is well approximated by a normal distribution with mean γ and standard deviation $\sqrt{\gamma}$. If we require that out of all voxels, at most

one spurious detection occurs on average, it follows that

$$\int_{-\infty}^{x} dx' \frac{1}{2\pi} e^{-x'^2} = 1 - \frac{V_{\text{vox}}}{V}, \qquad \text{(A4)}$$

where x sets the number of standard deviations needed. If we have D preexisting color centers and each color center creates p_1 photons, then the number of photons from one additional color center needs to exceed the standard deviation of $p_1 D$ photons from the preexisting color centers by a factor x:

$$\frac{p_1}{\sqrt{p_1 D}} = x \quad \text{or} \quad p_1 = 2D \, \text{erfc}^{-1} \left(2 - 2\frac{V_{\text{vox}}}{V} \right)^2, \quad \text{(A5)}$$

where erfc^{-1} is the inverse complementary error function. Note that erfc^{-1} has only a logarithmic dependence on V_{vox}/V. To obtain the number of photons that are needed to excite the fluorescence at rate p_1, we need to divide p_1 by the area A of the beam or light sheet, which is given by $A = v_z \sqrt{\text{f.o.v.}}$, where the field of view, f.o.v., is the area that is imaged at one time, assuming that f.o.v. is quadratic. We then require $p_1/A = p$ and can solve for fluence ϕ. Note that not every voxel needs to receive the fluence ϕ separately, since the sample is still optically thin, i.e., only a small fraction of fluorescence photons is absorbed in each voxel.

Finally, we need to consider time: the number of separate images taken of the volume V is $V/(\text{f.o.v.} v_z)$ and thus the time t per image is the $t = T(\text{f.o.v.} v_z)/V$, where T is the time allotted to scan all of the volume T. The remaining step is to multiply the result by the energy of each photon hc/λ. We obtain, for the beam power of the exciting laser for a total volume of 1 cm^3 and for $T = 1$ day,

$$P = 0.4 \, \text{W} \left(\frac{V_{\text{vox}}}{\mu \text{m}^3} \right) \left(\frac{10^6 \, \mu \text{m}^2}{\text{f.o.v.}} \right)^{1/2} \left(\frac{f_d}{10^{-10}} \right)$$

$$\times \left(\frac{\rho}{10 \, \text{g cm}^{-3}} \right) \left(\frac{1}{\xi} \right) \left(\frac{150 \, \text{g mol}^{-1}}{M} \right) \left(\frac{250 \, \text{nm}}{\lambda} \right)$$

$$\times \left(\frac{1.5}{\text{NA}} \right)^2 \left(\frac{0.8}{\epsilon} \right) f \left(\frac{V_{\text{vox}}}{V} \right), \qquad \text{(A6)}$$

where $P \propto V/T$ and $f(x) \simeq -0.0954 - 0.0912 \log_{10} x$, where the latter arises from expanding Eq. (A5) around $V_{\text{vox}}/V = 10^{-12}$.

4. Heat

The laser beam has a cross section of $\sqrt{\text{f.o.v.}} v_z$ and per unit depth into the sample deposits a fraction of the beam power proportional to the absorption coefficient α, i.e., $P\alpha$, which results in a uniform planar heat input, again assuming that the sample is optically thin. Heat conduction then

yields a temperature difference perpendicular to the beam of $\Delta T = P\alpha/\lambda\, d$, where d is the thickness of the sample; here, we assume that $v_z \ll d$, so that we effectively have a one-dimensional heat conduction problem. In appropriate units, this becomes

$$\Delta T = 1\,\mathrm{K}\left(\frac{P}{\mathrm{W}}\right)\left(\frac{10\,\mathrm{W\,K^{-1}\,m^{-1}}}{\lambda}\right)\left(\frac{\alpha}{0.1\mathrm{cm^{-1}}}\right)\left(\frac{d}{\mathrm{cm}}\right). \tag{A7}$$

The amount of heating is small because our samples are essentially transparent and reasonable heat conductors.

5. Data

The data volume B is given as the number of pixels per image f.o.v./v_x/v_y times the number of images taken $V/(\mathrm{f.o.v.}v_z)$:

$$B = 2\,\mathrm{TByte}\left(\frac{V}{1\,\mathrm{cm^2}}\right)\left(\frac{\mu\mathrm{m^3}}{V_{\mathrm{vox}}}\right)\left(\frac{b_d}{16\,\mathrm{bit}}\right), \tag{A8}$$

where b_d is the bit depth of the image.

6. Discussion

The required mechanical performance is demonstrated by existing light-sheet microscopes. We derive some simple scaling laws for the required laser power, the resulting heating, and the data volume. In the presence of preexisting color centers, decreasing the voxel volume is a way to keep the required power limited, demonstrating the advantage of voxelization over total-volume fluorescence. The laser power is further kept small by imaging an entire field of view at once, in contrast to confocal microscopy, reducing the power by 3–4 orders of magnitude. As a result, heating is generally very mild once heat conduction and the very small optical absorption of the samples are accounted for. The resulting data volume is significant but not does not seem to present a major obstacle. Consider a specific example of 100 g of BaF_2 to be scanned in 1 day with a preexisting color-center concentration of $f_d = 10^{-10}$ and an excitation wavelength of 250 nm [45]. BaF_2 has a density of 4.88 g cm^{-3} and a molecular weight of 137.3 u (see Table I). Using $V_{\mathrm{vox}} = 1\ \mu\mathrm{m^3}$, we obtain $P = 4.89$ W [Eq. (A6)]. The heat conductivity of BaF_2 $\lambda = 7.1$ W m^{-1} K^{-1} and the absorption coefficient around 250 nm is 0.2 cm^{-1} [87]. This results in $\Delta T = 13.8$ K for a 1-cm-thick sample from Eq. (A7). Note that, in practice, a thinner sample would be preferred from an optical point of view related to the working distance of high-performance microscope objectives. For instance, taking a Nikon CFI Apo LWD Lambda S 20XC WI [88] objective as an example, it has a working distance of just above 1 mm (0.9–0.99 mm plus 0.11–0.23 mm allowance for the cover slip) and a numerical aperture of NA=0.95. In this case, the power is

increased by $(1.5/0.95)^2$ to 12.2 W. However, the sample could be as thin as 1 mm thick to allow for the whole volume to be scanned and thus the temperature rise would be $\Delta T = 3.4$ K. A 100-g 1-mm-thick sample of BaF_2 would be approximately 15×15 cm^2. Finally, utilizing Eq. (A8), we find that the data volume for this example is approximately 41 TByte. We find similar numbers for the other materials listed in Table I.

In synopsis, none of the parameters used here appear to be extreme or problematic, with the key figure of merit being f_d/ξ, i.e., the ratio of the preexisting color-center density to the oscillator strength. With BaF_2 having a melting point of 1600 K (see Table I), a value of $\Delta T \simeq 340$ K, 2 orders of magnitude higher than the value found using the above parameters, still seems acceptable, so there is considerable headroom in our estimate.

[1] A. Drukier and L. Stodolsky, Principles and applications of a neutral-current detector for neutrino physics and astronomy, Phys. Rev. D **30**, 2295 (1984).

[2] M. W. Goodman and E. Witten, Detectability of certain dark matter candidates, Phys. Rev. D **31**, 3059 (1985).

[3] M. Battaglieri, A. Belloni, A. Chou, P. Cushman, B. Echenard, R. Essig, J. Estrada, J. L. Feng, B. Flaugher, and P. J. Fox *et al.*, in *U.S. Cosmic Visions: New Ideas in Dark Matter* (2017) arXiv:1707.04591 [hep-ph].

[4] D. Z. Freedman, Coherent neutrino nucleus scattering as a probe of the weak neutral current, Phys. Rev. D **9**, 1389 (1974).

[5] D. Akimov, J. Albert, P. An, C. Awe, P. Barbeau, B. Becker, V. Belov, A. Brown, A. Bolozdynya, and B. Cabrera-Palmer *et al.*, (COHERENT), Observation of coherent elastic neutrino-nucleus scattering, Science **357**, 1123 (2017).

[6] H. Bonet, A. Bonhomme, C. Buck, K. Fülber, J. Hakenmüller, G. Heusser, T. Hugle, M. Lindner, W. Maneschg, T. Rink, H. Strecker, and R. Wink, (CONUS), Constraints on Elastic Neutrino Nucleus Scattering in the Fully Coherent Regime from the CONUS Experiment, Phys. Rev. Lett. **126**, 041804 (2021).

[7] G. Agnolet, W. Baker, D. Barker, R. Beck, T. Carroll, J. Cesar, P. Cushman, J. Dent, S. D. Rijck, and B. Dutta *et al.*, (MINER), Background studies for the MINER coherent neutrino scattering reactor experiment, Nucl. Instrum. Meth. A **853**, 53 (2017).

[8] J. Rothe, G. Angloher, F. Ardellier-Desages, A. Bento, L. Canonic, A. Erhart, N. Ferreiro, M. Friedl, V. Ghete, and D. Hauff *et al.*, (NUCLEUS), NUCLEUS: Exploring coherent neutrino-nucleus scattering with cryogenic detectors, J. Low Temp. Phys. **199**, 433 (2019).

[9] D. Y. Akimov, V. Belov, A. Bolozdynya, Y. V. Efremenko, A. Etenko, A. Galavanov, D. Gouss, Y. V. Gusakov, D. E. Kdib, and A. Khromov *et al.*, (RED-100), First ground-level laboratory test of the two-phase xenon emission detector RED-100, JINST **15** (02), P02020. arXiv:1910.06190 [physics.ins-det].

[10] J. J. Choi, (NEON), Neutrino elastic-scattering observation with NaI[Tl], PoS **NuFact2019**, 047 (2020).

[11] J. Billard, R. Carr, J. Dawson, E. Figueroa-Feliciano, J. Formaggio, J. Gascon, S. Heine, M. D. Jesus, J. Johnston, T. Lasserre, A. Leder, K. Palladino, V. Sibille, M. Vivier, and L. Winslow, Coherent neutrino scattering with low temperature bolometers at Chooz reactor complex, J. Phys. G **44**, 105101 (2017).

[12] H. T.-K. Wong, (TEXONO), Taiwan EXperiment on neutrinO—history and prospects, The Universe **3**, 22 (2015).

[13] A. Aguilar-Arevalo, X. Bertou, C. Bonifazi, G. Cancelo, A. Castañeda, B. C. Vergara, C. Chavez, J. C. D'Olivo, J. C. D. Anjos, and J. Estrada *et al.*, (CONNIE), Exploring low-energy neutrino physics with the coherent neutrino nucleus interaction experiment, Phys. Rev. D **100**, 092005 (2019).

[14] A. de Gouvea, V. de Romeri, and C. A. Ternes, Probing neutrino quantum decoherence at reactor experiments, JHEP **08**, 018 (2020).

[15] G. Fernandez-Moroni, P. A. N. Machado, I. Martinez-Soler, Y. F. Perez-Gonzalez, D. Rodrigues, and S. Rosauro-Alcaraz, The physics potential of a reactor neutrino experiment with skipper CCDs: Measuring the weak mixing angle, JHEP **03**, 186 (2021).

[16] O. G. Miranda, D. K. Papoulias, M. Tórtola, and J. W. F. Valle, Probing new neutral gauge bosons with CEνNS and neutrino-electron scattering, Phys. Rev. D **101**, 073005 (2020).

[17] O. G. Miranda, D. K. Papoulias, O. Sanders, M. Tórtola, and J. W. F. Valle, Future CEvNS experiments as probes of lepton unitarity and light-sterile neutrinos, Phys. Rev. D **102**, 113014 (2020).

[18] O. Tomalak, P. Machado, V. Pandey, and R. Plestid, Flavor-dependent radiative corrections in coherent elastic neutrino-nucleus scattering, JHEP **02**, 097 (2021).

[19] B. K. Cogswell and P. Huber, Detection of breeding blankets using antineutrinos, Sci. Global Security **24**, 114 (2016).

[20] A. Bernstein, N. Bowden, B. L. Goldblum, P. Huber, I. Jovanovic, and J. Mattingly, *Colloquium*: Neutrino detectors as tools for nuclear security, Rev. Mod. Phys. **92**, 011003 (2020).

[21] M. Bowen and P. Huber, Reactor neutrino applications and coherent elastic neutrino nucleus scattering, Phys. Rev. D **102**, 053008 (2020).

[22] R. Essig, J. Mardon, O. Slone, and T. Volansky, Detection of sub-GeV dark matter and solar neutrinos via chemical-bond breaking, Phys. Rev. D **95**, 056011 (2017).

[23] S. Baum, A. K. Drukier, K. Freese, M. Górski, and P. Stengel, Searching for dark matter with paleo-detectors, Phys. Lett. B **803**, 135325 (2020).

[24] T. D. P. Edwards, B. J. Kavanagh, C. Weniger, S. Baum, A. K. Drukier, K. Freese, M. Górski, and P. Stengel, Digging for dark matter: Spectral analysis and discovery potential of paleo-detectors, Phys. Rev. D **99**, 043541 (2019).

[25] R. Budnik, O. Chesnovsky, O. Slone, and T. Volansky, Direct detection of light dark matter and solar neutrinos via color center production in crystals, Phys. Lett. B **782**, 242 (2018).

[26] S. Rajendran, N. Zobrist, A. O. Sushkov, R. Walsworth, and M. Lukin, A method for directional detection of dark matter using spectroscopy of crystal defects, Phys. Rev. D **96**, 035009 (2017).

[27] M. W. Doherty, N. B. Manson, P. Delaney, F. Jelezko, J. Wrachtrup, and L. C. Hollenberg, The nitrogen-vacancy colour centre in diamond, Phys. Rep. **528**, 1 (2013).

[28] R. Schirhagl, K. Chang, M. Loretz, and C. L. Degen, Nitrogen-vacancy centers in diamond: Nanoscale sensors for physics and biology, Annu. Rev. Phys. Chem. **65**, 83 (2014).

[29] Y. Wan, K. McDole, and P. J. Keller, Light-sheet microscopy and its potential for understanding developmental processes, Annu. Rev. Cell. Dev. Biol. **35**, 655 (2019).

[30] Excess workshop (2021), https://indico.cern.ch/event/1013203/.

[31] R. Ilić and S. A. Durrani, in *Handbook of Radioactivity Analysis*, edited by M. F. L'Annunziata (Academic Press, San Diego, 2003) 2nd ed., p. 179.

[32] S. Baum, T. D. P. Edwards, B. J. Kavanagh, P. Stengel, A. K. Drukier, K. Freese, M. Górski, and C. Weniger, Paleodetectors for galactic supernova neutrinos, Phys. Rev. D **101**, 103017 (2020).

[33] N. T. Arellano and S. Horiuchi, Measuring solar neutrinos over gigayear timescales with paleo detectors (2021).

[34] J. R. Jordan, S. Baum, P. Stengel, A. Ferrari, M. C. Morone, P. Sala, and J. Spitz, Measuring Changes in the Atmospheric Neutrino Rate over Gigayear Timescales, Phys. Rev. Lett. **125**, 231802 (2020).

[35] J. Ziegler, M. Ziegler, and J. Biersack, The stopping and range of ions in matter, NIM B **268**, 1818 (2010).

[36] K. Nordlund, S. J. Zinkl, A. E. Sand, F. Granberg, R. S. Averback, R. E. Stoller, T. Suzudo, L. Malerb, F. Banhart, W. J.Weber, F. Willaim, S. L.Dudarev, and David Simeonek, Primary radiation damage: A review of current understanding and models, J. Nucl. Mater. **512**, 450 (2018).

[37] G. H. Kinchin and R. S. Pease, The displacement of atoms in solids by radiation, Rep. Prog. Phys. **18**, 1 (1955).

[38] S. Chen and D. Bernard, On the calculation of atomic displacements using damage energy, Results Phys. **16**, 102835 (2020).

[39] For dark-matter searches this implies that we cannot study a diurnal modulation signal.

[40] ASTM E521—Standard practice for investigating effects of neutron radiation damage using charged-particle irradiation (2016), ASTM International, West Conshohocken, Pennsylvania.

[41] A. Y. Konobeyev, U. Fischer, Y. A. Korovin, and S. P. Simakov, Evaluation of effective threshold displacement energies and other data required for the calculation of advanced atomic displacement cross-sections, Nucl. Energy Technol. **3**, 169 (2017).

[42] K. Masuda, E. Vaughan, L. Arissian, J. Hendrie, J. Cole, J.-C. Diels, and A. Hecht, Novel techniques for high precision refractive index measurements, and application to assessing neutron damage and dose in crystals, NIM A **784**, 198 (2015).

[43] S. Plimpton, Fast parallel algorithms for short-range molecular dynamics, J. Comput. Phys. **117**, 1 (1995).

[44] J. Morris, B. Cowen, S. Teysseyre, and A. Hecht, Molecular dynamics investigation of threshold displacement energies in CaF_2, Comput. Mater. Sci. **172**, 109293 (2020).

[45] Y. Mosbacher, M. Weiss, H. Landsman, N. Priel, I. Eliyahu, A. Kreisel, O. Ozeri, D. Hershkovich, O. Cheshnovsky, and R. Budnik, Wide band spectroscopic response of monocrystallines to low dose neutron and gamma radiation, (2019).

[46] A. Häußler, P. Heller, L. P. McGuinness, B. Naydenov, and F. Jelezko, Optical depth localization of nitrogen-vacancy centers in diamond with nanometer accuracy, Opt. Express. **22**, 29986 (2014).

[47] J. Huisken, J. Swoger, F. Del Bene, J. Wittbrodt, and E. H. K. Stelzer, Optical sectioning deep inside live embryos by selective plane illumination microscopy, Science **305**, 1007 (2004).

[48] R. Tomer, M. Lovett-Barron, I. Kauvar, A. Andalman, V. Burns, S. Sankaran, L. Grosenick, M. Broxton, S. Yang, and K. Deisseroth, SPED light sheet microscopy: Fast mapping of biological system structure and function, Cell **163**, 1796 (2015).

[49] K. Shimizu, Color centers in sodium iodide, Rev. Phys. Chem. Jpn. **26**, 48 (1956).

[50] P. Avakatan and A. Smakula, Color centers in cesium halide single crystals, Phys. Rev. D **120**, 2007 (1960).

[51] S. Baccaro, P. Bohacek, A. Cecilia, V. Laguta, M. Montecchi, E. Mihokova, and M. Nikl, Effect of La doping on calcium tungstate ($CaWO_4$) crystals radiation hardness, Phys. Status Solidi A **178**, 799 (2000).

[52] D. Grigoriev, R. Akhmetshin, E. Babichev, Y. Borovlev, I. Chistokhin, N. Ivannikova, V. Kazanin, G. Kuznetsov, A. Postupaeva, V. Shlegel, and Y. Vasiliev, in *2013 IEEE Nuclear Science Symposium and Medical Imaging Conference (2013 NSS/MIC)* (2013), p. 1.

[53] E. Behnke, M. Besnier, P. Bhattacharjee, X. Daib, M. Das, A. Davour, F. Debris, N. Dhunganae, J. Farine, and M. Fines-Neuschild *et al.*, Final results of the PICASSO dark matter search experiment, Astropart. Phys. **90**, 85 (2017).

[54] J. D. Lewin and P. F. Smith, Review of mathematics, numerical factors, and corrections for dark matter experiments based on elastic nuclear recoil, Astropart. Phys. **6**, 87 (1996).

[55] R. W. Schnee, in *Theoretical Advanced Study Institute in Elementary Particle Physics: Physics of the Large and the Small* (2011).

[56] A. Abdelhameed, G. Angloher, P. Bauer, A. Bento, E. Bertoldo, C. Bucci, L. Canonica, A. D'Addabbo, X. Defay, and S. D. Lorenzo *et al.*, (CRESST), First results on sub-GeV spin-dependent dark matter interactions with ^7Li, Eur. Phys. J. C **79**, 630 (2019).

[57] L. Barak, I. M. Bloch, M. Cababie, G. Cancelo, L. Chaplinsky, F. Chierchie, M. Crisler, A. Drlica-Wagner, R. Essig, and J. Estrada *et al.*, (SENSEI), SENSEI: Direct-Detection Results on sub-GeV Dark Matter from a New Skipper-CCD, Phys. Rev. Lett. **125**, 171802 (2020).

[58] D. Amaral, T. Aralis, T. Aramaki, I. Arnquist, E. Azadbakht, S. Banik, D. Barker, C. Bathurst, D. Bauer, and L. Bezerra *et al.*, (SuperCDMS), Constraints on low-mass, relic dark matter candidates from a surface-operated super-CDMS single-charge sensitive detector, Phys. Rev. D **102**, 091101 (2020).

[59] T. Saab and E. Figueroa, Dark limit plotter, sc mathematica package.

[60] M. Felizardo, T. A. Girard, T. Morlat, A. C. Fernandes, A. R. Ramos, J. G. Marques, A. Kling, J. Puibasset, M. Auguste, and D. Boyer *et al.*, (SIMPLE Collaboration), Final Analysis and Results of the Phase II SIMPLE Dark Matter Search, Phys. Rev. Lett. **108**, 201302 (2012).

[61] D. Akerib, S. Alsum, H. Araújo, X. Bai, A. Bailey, J. Balajthy, P. Beltrame, E. Bernard, A. Bernstein, and T. Biesiadzinski *et al.*, Limits on Spin-Dependent WIMP-Nucleon Cross Section Obtained from the Complete LUX Exposure, Phys. Rev. Lett. **118**, 251302 (2017).

[62] C. Fu, X. Cui, X. Zhou, X. Chen, Y. Chen, D. Fang, K. Giboni, F. Giuliani, K. Han, and X. Huang *et al.*, Spin-Dependent Weakly-Interacting-Massive-Particle—Nucleon Cross Section Limits from First Data of PandaX-II Experiment, Phys. Rev. Lett. **118**, 071301 (2017).

[63] E. Aprile, J. Aalbers, F. Agostini, M. Alfonsi, F. D. Amaro, M. Anthony, F. Arneodo, P. Barrow, L. Baudis, and B. Bauermeister *et al.*, XENON100 dark matter results from a combination of 477 live days, Phys. Rev. D **94**, 122001 (2016).

[64] R. Agnese, A. J. Anderson, T. Aramaki, I. Arnquist, W. Baker, D. Barker, R. B. Thakur, D. A. Bauer, A. Borgland, and M. A. Bowles *et al.*, (superCDMS Collaboration), Low-mass dark matter search with CDMSlite, Phys. Rev. D **97**, 022002 (2018).

[65] C. Amole, M. Ardid, I. J. Arnquist, D. M. Asner, D. Baxter, E. Behnke, M. Bressler, B. Broerman, G. Cao, and C. J. Chen *et al.*, (PICO), Dark matter search results from the complete exposure of the PICO-60 C_3F_8 bubble chamber, Phys. Rev. D **100**, 022001 (2019).

[66] S. Olson, Master's thesis, Department of Physics, Engineering Physics and Astronomy, Queen's University, Ontario (2018).

[67] E. Vitagliano, I. Tamborra, and G. Raffelt, Grand unified neutrino spectrum at Earth: Sources and spectral components, Rev. Mod. Phys. **92**, 45006 (2020).

[68] J. Billard, L. Strigari, and E. Figueroa-Feliciano, Implication of neutrino backgrounds on the reach of next generation dark matter direct detection experiments, Phys. Rev. D **89**, 023524 (2014).

[69] P. Huber, On the determination of anti-neutrino spectra from nuclear reactors, Phys. Rev. C **84**, 024617 (2011), [Erratum: Phys.Rev.C 85, 029901 (2012)].

[70] M. Bergevin, N. Bowden, H. P. Mumm, M. Verstraeten, J. Park, B. Han, Y. Shitov, A. Serebrov, A. Onillon, G. Karagiorgi, and K. Nakajima *et al.*, Applied antineutrino physics 2018 proceedings (2019), presentation by the PROSPECT collaboration.

[71] J. Hakenmüller, First constraints on coherent elastic neutrino nucleus scattering by CONUS (2020), Magnificent CEvNS.

[72] R. Cerulli, NUCLEUS (2020), Magnificent CEvNS.

[73] P. Mota, CONNIE (2020), Magnificent CEvNS.

[74] T. Salagnac, RICOCHET (2020), Magnificent CEvNS.

[75] R. Mahapatra, MINER (2020), Magnificent CEvNS.

[76] A. A. Borovoi and L. A. Mikaelyan, Possibilities of the practical use of neutrinos, Soviet Atomic Energy **44**, 589 (1978).

[77] J. Ashenfelter, A. Balantekin, C. Baldenegro, H. Band, C. Bass, D. Bergeron, D. Berish, L. Bignell, N. Bowden, and J. Bricco *et al.*, (PROSPECT), First Search for Short-Baseline Neutrino Oscillations at HFIR with PROSPECT, Phys. Rev. Lett. **121**, 251802 (2018).

[78] A. Haghighat, P. Huber, S. Li, J. M. Link, C. Mariani, J. Park, and T. Subedi, Observation of Reactor Antineutrinos with a Rapidly-Deployable Surface-Level Detector, Phys. Rev. Appl. **13**, 034028 (2020).

[79] IAEA, *Proceedings of the first meeting of the Ad Hoc Working Group on Safeguards Applications utilizing Antineutrino Detection and Monitoring*, Tech. Rep. (2012).

[80] IAEA, *Safeguards Techniques and Equipment:*, International Nuclear Verification Series No. 1 (Rev. 2) (International Atomic Energy Agency, Vienna, 2011).

[81] IAEA, *Safeguards Glossary*, International Nuclear Verification Series No. 3 (International Atomic Energy Agency, Vienna, 2001).

[82] E. Christensen, P. Huber, P. Jaffke, and T. E. Shea, Antineutrino Monitoring for Heavy Water Reactors, Phys. Rev. Lett. **113**, 042503 (2014).

[83] M. Zendel, D. L. Donohue, E. Kuhn, S. Deron, and T. Biro, Nuclear safeguards verification measurement techniques, Handbook of Nuclear Chemistry (2011).

[84] S. Philippe and F. d'Errico, A physical unclonable neutron sensor for nuclear arms control inspections, Sci. Rep. **10**, 20605 (2020).

[85] A. Glaser, B. Barak, and R. Goldston, A zero-knowledge protocol for nuclear warhead verification, Nature **510**, 497 (2014).

[86] S. Philippe, R. Goldston, A. Glaser, and F. d'Errico, A physical zero-knowledge object-comparison system for nuclear warhead verification, Nat. Commun. **7**, 12890 (2016).

[87] https://www.lakeshore.com/docs/default-source/default-document-library/barium-fluoride-baf2-transmission-curve-datasheet.pdf?sfvrsn=bc1b2647_2, accessed 10/15/21.

[88] https://www.microscope.healthcare.nikon.com/products/optics/selector/comparison/-1918, accessed 10/15/21.